

Local Characteristic Decomposition of Equilibrium Variables for Hyperbolic Systems of Balance Laws

Shaoshuai Chu*, Alexander Kurganov†, Mingye Na‡ and Ruixiao Xin§

Abstract

This paper is concerned with high-order numerical methods for hyperbolic systems of balance laws. Such methods are typically based on high-order piecewise polynomial reconstructions (interpolations) of the computed discrete quantities. However, such reconstructions (interpolations) may be oscillatory unless the reconstruction (interpolation) procedure is applied to the local characteristic variables via the local characteristic decomposition (LCD). Another challenge in designing accurate and stable high-order schemes is related to enforcing a delicate balance between the fluxes, sources, and nonconservative product terms: a good scheme should be well-balanced (WB) in the sense that it should be capable of exactly preserving certain (physically relevant) steady states. One of the ways to ensure that the reconstruction (interpolation) preserves these steady states is to apply the reconstruction (interpolation) to the equilibrium variables, which are supposed to be constant at the steady states. To achieve this goal and to keep the reconstruction (interpolation) non-oscillatory, we introduce a new LCD of equilibrium variables. We apply the developed technique to the fifth-order Ai-WENO-Z interpolation implemented within the WB A-WENO framework recently introduced in [S. Chu, A. Kurganov, and R. Xin, Beijing J. of Pure and Appl. Math., to appear], and illustrate its performance on a variety of numerical examples.

Key words: High-order reconstruction (interpolation), A-WENO schemes, well-balanced schemes, equilibrium variables, local characteristic decomposition.

AMS subject classification: 76M20, 65M06, 35L65, 35L67.

1 Introduction

This paper is focused on the development of a new local characteristic decomposition (LCD) of equilibrium variables for hyperbolic systems of balance laws which, in the one-dimensional (1-D)

*Department of Mathematics, RWTH Aachen University, 52056 Aachen, Germany; chuss2019@mail.sustech.edu.cn

†Department of Mathematics, Shenzhen International Center for Mathematics, and Guangdong Provincial Key Laboratory of Computational Science and Material Design, Southern University of Science and Technology, Shenzhen, 518055, China; alexander@sustech.edu.cn

‡Department of Mathematics, Southern University of Science and Technology, Shenzhen, 518055, China; 12131231@mail.sustech.edu.cn

§Department of Mathematics, Southern University of Science and Technology, Shenzhen, 518055, China; 12331009@mail.sustech.edu.cn

case, read as

$$\mathbf{U}_t + \mathbf{F}(\mathbf{U})_x = B(\mathbf{U})\mathbf{U}_x + \mathbf{S}(\mathbf{U}). \quad (1.1)$$

Here, x is the spatial variable, t is time, $\mathbf{U} \in \mathbb{R}^d$ is a vector of unknowns, $\mathbf{F}, \mathbf{S} : \mathbb{R}^d \rightarrow \mathbb{R}^d$ are the flux and source terms, and $B \in \mathbb{R}^{d \times d}$.

Development of high-order numerical methods for (1.1) is a challenging task for the following two main reasons. First, solutions of (1.1) may develop discontinuities (even for infinitely smooth initial data) and thus high-order schemes should rely on non-oscillatory high-order reconstructions (interpolations) of the solutions out of the computed discrete quantities. To make these reconstructions (interpolations) non-oscillatory, one typically needs to use nonlinear limiting techniques often applied to the local characteristic variables via the LCD; see, e.g., [6, 10, 11, 14, 16–18, 22]. The LCD is applied by computing the local values of the Jacobian $\partial \mathbf{F} / \partial \mathbf{U}$, locally switching to the corresponding characteristic variables, performing the reconstruction (interpolation) to these local variables, and then switching back to the original variables \mathbf{U} .

Second, many (physically relevant) solutions of (1.1) are, in fact, small perturbations of certain steady states, which are supposed to be exactly preserved by good high-order schemes—this is a so-called well-balanced (WB) property. One of the ways to ensure that the high-order reconstruction (interpolation) preserves these steady states is to reconstruct (interpolate) the equilibrium variables instead of the conservative ones. We note that in many cases, the equilibrium variables can be obtained by rewriting the system (1.1) in the following form (see [12]):

$$\mathbf{U}_t + M(\mathbf{U})\mathbf{E}(\mathbf{U})_x = \mathbf{0}, \quad (1.2)$$

where

$$M(\mathbf{U})\mathbf{E}(\mathbf{U})_x = \mathbf{F}(\mathbf{U})_x - B(\mathbf{U})\mathbf{U}_x - \mathbf{S}(\mathbf{U}), \quad (1.3)$$

which vanishes at steady states. In (1.3), $M \in \mathbb{R}^{d \times d}$ and \mathbf{E} is the vector of equilibrium variables, which are constant at steady states. Therefore, one may prefer to reconstruct the equilibrium variables \mathbf{E} instead of \mathbf{U} since in this case, all of the reconstructed values of \mathbf{E} will be also constant at steady states. However, applying the LCD approach, which is based on the Jacobian $\partial \mathbf{F} / \partial \mathbf{U}$ and not on the equilibrium variables, may destroy the WB property of the resulting scheme.

In this paper, we introduce a new LCD of equilibrium variables. To this end, we first rewrite the system (1.2) in the following equivalent (for smooth solution) form:

$$\mathbf{E}(\mathbf{U})_t + C(\mathbf{U})\mathbf{E}(\mathbf{U})_x = \tilde{\mathbf{I}}(\mathbf{U}), \quad (1.4)$$

where the matrix C and the source term $\tilde{\mathbf{I}}$ are specified in §3. We then compute the matrices C at the grid points and use them to compute the local characteristic equilibrium variables, which are reconstructed (interpolated) to obtain high-order values of \mathbf{E} , which, in turn, give us the corresponding high-order values of \mathbf{U} (solving nonlinear systems of equations may be required). We implement the new LCD technique in the framework of flux globalization based WB alternative weighted essentially non-oscillatory (A-WENO) finite-difference schemes recently introduced in [5]. The local characteristic equilibrium variables are interpolated using the fifth-order affine-invariant WENO-Z (Ai-WENO-Z) interpolations [7, 13, 19]. The developed A-WENO scheme is applied to three systems of balance laws including the nozzle flow system and the one- and two-layer shallow water equations. We conduct several numerical experiments to demonstrate the performance of the proposed scheme.

2 Flux Globalization Based WB A-WENO Schemes: An Overview

In this section, we give an overview of the flux globalization based WB A-WENO schemes introduced in [5] for general nonconservative systems (1.1), which can be written in an equivalent quasi-conservative form:

$$\mathbf{U}_t + \mathbf{K}(\mathbf{U})_x = \mathbf{0},$$

where $\mathbf{K}(\mathbf{U})$ is a global flux

$$\mathbf{K}(\mathbf{U}) = \mathbf{F}(\mathbf{U}) - \mathbf{R}(\mathbf{U}), \quad \mathbf{R}(\mathbf{U}) = \int_{\hat{x}}^x \left[B(\mathbf{U}(\xi, t)) \mathbf{U}_\xi(\xi, t) + \mathbf{S}(\mathbf{U}(\xi, t)) \right] d\xi,$$

and \hat{x} is an arbitrary number.

We first introduce a uniform mesh consisting of the cells $[x_{j-\frac{1}{2}}, x_{j+\frac{1}{2}}]$ of size $x_{j+\frac{1}{2}} - x_{j-\frac{1}{2}} \equiv \Delta x$ centered at $x_j = (x_{j-\frac{1}{2}} + x_{j+\frac{1}{2}})/2$, $j = 1, \dots, N$. We assume that at a certain time level t , the approximate solution, realized in terms of its cell centered values $\mathbf{U}_j \approx \mathbf{U}(x_j, t)$, is available (in the rest of the paper, we will suppress the time-dependence of all of the indexed quantities for the sake of brevity). The solution is then evolved in time by solving the following system of ODEs:

$$\frac{d\mathbf{U}_j}{dt} = -\frac{\mathcal{K}_{j+\frac{1}{2}} - \mathcal{K}_{j-\frac{1}{2}}}{\Delta x}, \quad (2.1)$$

where $\mathcal{K}_{j+\frac{1}{2}}$ are the fifth-order A-WENO numerical fluxes (see [2, 10, 14, 20–22]):

$$\mathcal{K}_{j+\frac{1}{2}} = \mathcal{K}_{j+\frac{1}{2}}^{\text{FV}} - \frac{(\Delta x)^2}{24} (\mathbf{K}_{xx})_{j+\frac{1}{2}} + \frac{7(\Delta x)^4}{5760} (\mathbf{K}_{xxxx})_{j+\frac{1}{2}}.$$

Here, $\mathcal{K}_{j+\frac{1}{2}}^{\text{FV}}$ is a finite-volume numerical flux (in the numerical experiments reported in §4, we have used the second-order WB path-conservative central-upwind numerical flux introduced in [12]), and $(\mathbf{K}_{xx})_{j+\frac{1}{2}}$ and $(\mathbf{K}_{xxxx})_{j+\frac{1}{2}}$ are the high-order correction terms. The numerical fluxes $\mathcal{K}_{j+\frac{1}{2}}^{\text{FV}} = \mathcal{K}_{j+\frac{1}{2}}^{\text{FV}}(\mathbf{U}_{j+\frac{1}{2}}^\pm, \widehat{\mathbf{U}}_{j+\frac{1}{2}}^\pm)$ are computed using the one-sided interpolated values of \mathbf{U} , and to enforce the WB evolution, one needs to use two copies of those values denoted by $\mathbf{U}_{j+\frac{1}{2}}^\pm$ and $\widehat{\mathbf{U}}_{j+\frac{1}{2}}^\pm$; see [5, 12] for details. The correction terms $(\mathbf{K}_{xx})_{j+\frac{1}{2}}$ and $(\mathbf{K}_{xxxx})_{j+\frac{1}{2}}$ are computed using the numerical fluxes $\mathcal{K}_{j+\frac{1}{2}}^{\text{FV}}$, which have been already obtained:

$$\begin{aligned} (\mathbf{K}_{xx})_{j+\frac{1}{2}} &= \frac{1}{12(\Delta x)^2} \left[-\mathcal{K}_{j-\frac{3}{2}}^{\text{FV}} + 16\mathcal{K}_{j-\frac{1}{2}}^{\text{FV}} - 30\mathcal{K}_{j+\frac{1}{2}}^{\text{FV}} + 16\mathcal{K}_{j+\frac{3}{2}}^{\text{FV}} - \mathcal{K}_{j+\frac{5}{2}}^{\text{FV}} \right], \\ (\mathbf{K}_{xxxx})_{j+\frac{1}{2}} &= \frac{1}{(\Delta x)^4} \left[\mathcal{K}_{j-\frac{3}{2}}^{\text{FV}} - 4\mathcal{K}_{j-\frac{1}{2}}^{\text{FV}} + 6\mathcal{K}_{j+\frac{1}{2}}^{\text{FV}} - 4\mathcal{K}_{j+\frac{3}{2}}^{\text{FV}} + \mathcal{K}_{j+\frac{5}{2}}^{\text{FV}} \right]; \end{aligned}$$

see [4] for details.

3 Local Characteristic Decomposition of Equilibrium Variables

In this section, we apply the LCD approach introduced in [6,10,11,14,16–18,22] to the Ai-WENO-Z interpolation of the equilibrium variables.

We first need to specify C and $\tilde{\mathbf{I}}$ in (1.4). To this end, we consider two possible cases.

- If $\mathbf{E}(\mathbf{U})$ is a local quantity, then we simply multiply (1.2) by $\partial\mathbf{E}/\partial\mathbf{U}$ and obtain (1.4) with $C(\mathbf{U}) = \partial\mathbf{E}/\partial\mathbf{U}M(\mathbf{U})$ and $\tilde{\mathbf{I}}(\mathbf{U}) \equiv \mathbf{0}$
- If $\mathbf{E}(\mathbf{U})$ is a global quantity, which can be written as

$$\mathbf{E}(\mathbf{U}) = \mathbf{W}(\mathbf{U}) + \mathbf{I}(\mathbf{U}),$$

where $\mathbf{W}(\mathbf{U})$ is a local term and

$$\mathbf{I}(\mathbf{U}) = \int_{\hat{x}}^x \mathbf{G}(\mathbf{U}(\xi, t)) d\xi$$

with \hat{x} being an arbitrary number, then we proceed in a different way. We first multiply (1.2) by $\partial\mathbf{W}/\partial\mathbf{U}$ and then add $\mathbf{I}(\mathbf{U})_t$ to both sides of the resulting equation to obtain (1.4) with $C(\mathbf{U}) = \partial\mathbf{W}/\partial\mathbf{U}M(\mathbf{U})$ and $\tilde{\mathbf{I}}(\mathbf{U})$ computed as follows:

$$\begin{aligned} \mathbf{I}(\mathbf{U})_t &= \int_{\hat{x}}^x \mathbf{G}(\mathbf{U}(\xi, t))_t d\xi = \int_{\hat{x}}^x \frac{\partial\mathbf{G}}{\partial\mathbf{U}}(\mathbf{U}(\xi, t)) \mathbf{U}_t(\xi, t) d\xi \\ &= - \int_{\hat{x}}^x \frac{\partial\mathbf{G}}{\partial\mathbf{U}}(\mathbf{U}(\xi, t)) M(\mathbf{U}(\xi, t)) \mathbf{E}(\mathbf{U}(\xi, t))_x d\xi =: \tilde{\mathbf{I}}(\mathbf{U}). \end{aligned}$$

In fact, the details on $\tilde{\mathbf{I}}$ are not important as this source term does not influence the LCD of equilibrium variables, which is based on the matrix C only.

We then evaluate the matrix C at the grid points to obtain the constant matrices $C_j := C(\mathbf{U}_j)$, which can be diagonalized using the matrices Q_j and Q_j^{-1} to obtain $\Lambda_j = Q_j^{-1}C_jQ_j$, where Λ_j is a diagonal matrix containing the eigenvalues of C_j .

Next, we introduce the local characteristic equilibrium variables in the neighborhood of $x = x_j$:

$$\mathbf{\Gamma}_k = Q_j^{-1} \mathbf{E}_k, \quad k = j \pm 2, j \pm 1, j, \quad (3.1)$$

apply the fifth-order Ai-WENO-Z (or any other fifth-order WENO-type) interpolation to evaluate the values $\mathbf{\Gamma}_{j-\frac{1}{2}}^+$ and $\mathbf{\Gamma}_{j+\frac{1}{2}}^-$, and finally obtain

$$E_{j\mp\frac{1}{2}}^\pm = Q_j \mathbf{\Gamma}_{j\mp\frac{1}{2}}^\pm. \quad (3.2)$$

Equipped with these values, we proceed as in [5, 12] and solve the nonlinear equations (see [1, equations (2.8) and (2.16)]) to recover the values $\mathbf{U}_{j\mp\frac{1}{2}}^\pm$ and $\widehat{\mathbf{U}}_{j\mp\frac{1}{2}}^\pm$ needed to evaluate the numerical fluxes $\mathcal{K}_{j+\frac{1}{2}}^{\text{FV}}$.

Remark 3.1 It should be pointed out that the presented LCD-based reconstruction algorithm is different from the one used in, e.g., [3] as the LCD process is now performed at the cell centers $x = x_j$ not at the cell interfaces $x_{j+\frac{1}{2}}$. The current approach has three advantages. First, no averaged values of any quantities from cells j and $j+1$ are required. Second, only five—not six—values of $\mathbf{\Gamma}$ should be computed for every j . Third, we can use only one Ai-WENO-Z interpolant in every cell C_j to evaluate $\mathbf{\Gamma}_{j-\frac{1}{2}}^+$ and $\mathbf{\Gamma}_{j+\frac{1}{2}}^-$, while in the LCD algorithm in [3], one had to use two Ai-WENO-Z interpolants to compute the one-sided values of $\mathbf{\Gamma}_{j+\frac{1}{2}}^\pm$.

Next, we show the application of the introduced LCD of equilibrium variables to three particular systems of balance laws.

3.1 Application to the Nozzle Flow System

In this section, we consider the nozzle flow system, which reads as (1.1) with

$$\mathbf{U} = (\sigma\rho, \sigma\rho u)^\top, \quad \mathbf{F}(\mathbf{U}) = (\sigma\rho u, \sigma\rho u^2 + \sigma p)^\top, \quad B(\mathbf{U}) = 0, \quad \mathbf{S}(\mathbf{U}) = (0, p\sigma_x)^\top,$$

where ρ is the density, u is the velocity, $p(\rho) = \kappa\rho^\gamma$ is the pressure, $\kappa > 0$ and $1 < \gamma < \frac{5}{3}$ are constants, and $\sigma = \sigma(x)$ denotes the cross-section of the nozzle. The studied nozzle flow system admits steady-state solutions satisfying $M(\mathbf{U})\mathbf{E}(\mathbf{U})_x = \mathbf{0}$ with

$$M(\mathbf{U}) = \begin{pmatrix} 1 & 0 \\ u & \sigma\rho \end{pmatrix}, \quad \mathbf{E}(\mathbf{U}) = \begin{pmatrix} q \\ E \end{pmatrix}, \quad q = \sigma\rho u, \quad E = \frac{u^2}{2} + \frac{\kappa\gamma}{\gamma-1}\rho^{\gamma-1}.$$

In order to apply the fifth-order Ai-WENO-Z interpolation to the equilibrium variables, we first compute

$$E_j = \frac{u_j^2}{2} + \frac{\kappa\gamma}{\gamma-1}(\rho_j)^{\gamma-1},$$

where $u_j = q_j/(\sigma\rho)_j$, $\rho_j = (\sigma\rho)_j/\sigma_j$, and $\sigma_j = \sigma(x_j)$, and then evaluate the matrices

$$C_j = \begin{pmatrix} u_j & (\sigma\rho)_j \\ \frac{\kappa\gamma(\rho_j)^{\gamma-1}}{(\sigma\rho)_j} & u_j \end{pmatrix}, \quad Q_j = \begin{pmatrix} (\sigma\rho)_j & (\sigma\rho)_j \\ -\sqrt{\kappa\gamma}(\rho_j)^{\frac{\gamma-1}{2}} & \sqrt{\kappa\gamma}(\rho_j)^{\frac{\gamma-1}{2}} \end{pmatrix},$$

$$Q_j^{-1} = \frac{1}{2\sqrt{\kappa\gamma}(\sigma\rho)_j(\rho_j)^{\frac{\gamma-1}{2}}} \begin{pmatrix} \sqrt{\kappa\gamma}(\rho_j)^{\frac{\gamma-1}{2}} & -(\sigma\rho)_j \\ \sqrt{\kappa\gamma}(\rho_j)^{\frac{\gamma-1}{2}} & (\sigma\rho)_j \end{pmatrix}.$$

We now implement the LCD of the equilibrium variables followed by the fifth-order Ai-WENO-Z interpolation giving $\mathbf{\Gamma}_{j\mp\frac{1}{2}}^\pm$ and then $q_{j\mp\frac{1}{2}}^\pm$ and $E_{j\mp\frac{1}{2}}^\pm$. After that, we apply the same fifth-order Ai-WENO-Z interpolation to obtain the one-sided values of the cross-section of the nozzle $\sigma_{j\mp\frac{1}{2}}^\pm$, and then solve the nonlinear equations as described in [5, Equations (3.5) and (3.6)] to obtain $(\sigma\rho)_{j\mp\frac{1}{2}}^\pm$ and $(\widehat{\sigma\rho})_{j\mp\frac{1}{2}}^\pm$.

3.2 Application to the Saint-Venant System with Manning Friction

In this section, we consider the Saint-Venant system of shallow water equations with Manning friction, which reads as (1.1) with

$$\mathbf{U} = (h, q)^\top, \quad \mathbf{F}(\mathbf{U}) = \left(q, hu^2 + \frac{1}{2}gh^2\right)^\top, \quad B(\mathbf{U}) = 0, \quad \mathbf{S}(\mathbf{U}) = (0, -ghZ_x - ghS_f)^\top,$$

where h is the water depth, u is the velocity, $q = hu$ represents the discharge, $Z(x)$ is a function describing the bottom topography, which can be discontinuous, g is the constant acceleration due to gravity, S_f is the Manning friction term (see, e.g., [15]) given by $S_f = n^2 q |q| h^{-\frac{10}{3}}$. The studied Saint-Venant system admits steady-state solutions satisfying $M(\mathbf{U})\mathbf{E}(\mathbf{U})_x = \mathbf{0}$ with

$$M(\mathbf{U}) = \begin{pmatrix} 1 & 0 \\ u & h \end{pmatrix}, \quad \mathbf{E}(\mathbf{U}) = \begin{pmatrix} q \\ E \end{pmatrix}, \quad E = \frac{u^2}{2} + g(h + Z) + \int_{\hat{x}}^x gS_f d\xi.$$

In order to apply the fifth-order Ai-WENO-Z interpolation to the equilibrium variables, we first compute

$$E_j = \frac{u_j^2}{2} + g(h_j + Z_j) + I_j,$$

where $u_j = q_j/h_j$, $Z_j = Z(x_j)$, and I_j is an fifth-order approximation of the integral $\int_{x_{-\frac{5}{2}}}^{x_j} gS_f dx$, in which we have set $\hat{x} = x_{-\frac{5}{2}}$. The values I_j are computed as follows. First, we evaluate $(S_f)_j = n^2 q_j |q_j| h_j^{-\frac{10}{3}}$ for $j = 1, \dots, N$ and extend these values to $j = -5, \dots, 0$ and $j = N + 1, \dots, N + 5$ using the prescribed boundary conditions (for h and q) implemented within the ghost cell framework. We then construct the interpolating polynomial for S_f using the six points $(x_{-5}, (S_f)_{-5}), \dots, (x_0, (S_f)_0)$ and integrate it over the interval $[x_{-\frac{5}{2}}, x_{-2}]$ to obtain

$$I_{-2} = \frac{g\Delta x}{46080} \left[163(S_f)_{-5} - 1303(S_f)_{-4} + 6582(S_f)_{-3} + 19082(S_f)_{-2} - 1673(S_f)_{-1} + 189(S_f)_0 \right].$$

We then proceed recursively: construct the interpolating polynomials for S_f using $(x_{j-3}, (S_f)_{j-3}), \dots, (x_{j+2}, (S_f)_{j+2})$, integrate them over the corresponding interval $[x_{j-1}, x_j]$, and end up with

$$I_j = I_{j-1} + \frac{g\Delta x}{1440} \left[11(S_f)_{j-3} - 93(S_f)_{j-2} + 802(S_f)_{j-1} + 802(S_f)_j - 93(S_f)_{j+1} + 11(S_f)_{j+2} \right].$$

We then evaluate the matrices

$$C_j = \begin{pmatrix} u_j & h_j \\ g & u_j \end{pmatrix}, \quad Q_j = \begin{pmatrix} \sqrt{h_j} & \sqrt{h_j} \\ -\sqrt{g} & \sqrt{g} \end{pmatrix}, \quad Q_j^{-1} = \frac{1}{2\sqrt{gh_j}} \begin{pmatrix} \sqrt{g} & -\sqrt{h_j} \\ \sqrt{g} & \sqrt{h_j} \end{pmatrix},$$

and implement the LCD of the equilibrium variables followed by the fifth-order Ai-WENO-Z interpolation giving $\mathbf{\Gamma}_{j\mp\frac{1}{2}}^\pm$ and then $q_{j\mp\frac{1}{2}}^\pm$ and $E_{j\mp\frac{1}{2}}^\pm$. After that, we apply the same fifth-order Ai-WENO-Z interpolation to obtain the one-sided values of the bottom topography $Z_{j\mp\frac{1}{2}}^\pm$, and then solve the nonlinear equations

$$E_{j+\frac{1}{2}}^\pm = \frac{(q_{j+\frac{1}{2}}^\pm)^2}{2(h_{j+\frac{1}{2}}^\pm)^2} + g \left(h_{j+\frac{1}{2}}^\pm + Z_{j+\frac{1}{2}}^\pm \right) + I_{j+\frac{1}{2}}, \quad (3.3)$$

and

$$E_{j+\frac{1}{2}}^{\pm} = \frac{(q_{j+\frac{1}{2}}^{\pm})^2}{2(\widehat{h}_{j+\frac{1}{2}}^{\pm})^2} + g \left(\widehat{h}_{j+\frac{1}{2}}^{\pm} + Z_{j+\frac{1}{2}} \right) + I_{j+\frac{1}{2}}, \quad Z_{j+\frac{1}{2}} = \frac{1}{2} \left(Z_{j+\frac{1}{2}}^{+} + Z_{j+\frac{1}{2}}^{-} \right) \quad (3.4)$$

to obtain $h_{j+\frac{1}{2}}^{\pm}$ and $\widehat{h}_{j+\frac{1}{2}}^{\pm}$, respectively. Here, the integrals $I_{j+\frac{1}{2}}$ are evaluated recursively by the fifth-order quadrature: we first set $I_{-\frac{5}{2}} = 0$ and then compute

$$I_{j+\frac{1}{2}} = I_{j-\frac{1}{2}} + \frac{g\Delta x}{5760} \left[-17(S_f)_{j-2} + 308(S_f)_{j-1} + 5178(S_f)_j + 308(S_f)_{j+1} - 17(S_f)_{j+2} \right]$$

for $j = -2, \dots, N+2$, where we have used the quadrature, which is obtained by constructing the interpolating polynomials for S_f using the five points $(x_{j-2}, (S_f)_{j-2}), \dots, (x_{j+2}, (S_f)_{j+2})$ and integrating them over the corresponding intervals $[x_{j-\frac{1}{2}}, x_{j+\frac{1}{2}}]$. Notice that equations (3.3) and (3.4) are cubic and we solve them exactly as described in [1].

3.3 Application to the Two-Layer Shallow Water System

In this section, we consider the two-layer shallow water system, which reads as (1.1) with

$$\begin{aligned} \mathbf{U} &= (h_1, q_1, h_2, q_2)^{\top}, \\ \mathbf{F}(\mathbf{U}) &= (q_1, h_1 u_1^2 + \frac{g}{2} h_1^2, q_2, h_2 u_2^2 + \frac{g}{2} h_2^2)^{\top}, \quad B(\mathbf{U}) = \begin{pmatrix} 0 & 0 & 0 & 0 \\ 0 & 0 & -gh_1 & 0 \\ 0 & 0 & 0 & 0 \\ -rgh_2 & 0 & 0 & 0 \end{pmatrix}, \\ \mathbf{S}(\mathbf{U}) &= (0, -gh_1 Z_x, 0, -gh_2 Z_x)^{\top}, \end{aligned}$$

Here, h_1 and h_2 are the water depths in the upper and lower layers, respectively, u_1 and u_2 are the corresponding velocities, $q_1 = h_1 u_1$ and $q_2 = h_2 u_2$ represent the corresponding discharges, $Z(x)$ and g are the same as in §3.2, and $r = \frac{\rho_1}{\rho_2} < 1$ is the ratio of the constant densities ρ_1 (upper layer) and ρ_2 (lower layer). The studied two-layer shallow water system admits steady-state solutions satisfying $M(\mathbf{U})\mathbf{E}(\mathbf{U})_x = \mathbf{0}$ with

$$M(\mathbf{U}) = \begin{pmatrix} 1 & 0 & 0 & 0 \\ u_1 & h_1 & 0 & 0 \\ 0 & 0 & 1 & 0 \\ 0 & 0 & u_2 & h_2 \end{pmatrix}, \quad \mathbf{E}(\mathbf{U}) = \begin{pmatrix} q_1 \\ E_1 \\ q_2 \\ E_2 \end{pmatrix}, \quad \begin{aligned} E_1 &:= \frac{q_1^2}{2h_1^2} + g(h_1 + h_2 + Z), \\ E_2 &:= \frac{q_2^2}{2h_2^2} + g(rh_1 + h_2 + Z). \end{aligned}$$

In order to apply the fifth-order Ai-WENO-Z interpolation to the equilibrium variables, we first compute

$$\begin{aligned} (E_1)_j &= \frac{(q_1)_j^2}{2(h_1)_j^2} + g[(h_1)_j + (h_2)_j + Z_j], \\ (E_2)_j &= \frac{(q_2)_j^2}{2(h_2)_j^2} + g[r(h_1)_j + (h_2)_j + Z_j], \end{aligned}$$

and evaluate the matrices

$$C_j = \begin{pmatrix} (u_1)_j & (h_1)_j & 0 & 0 \\ g & (u_1)_j & g & 0 \\ 0 & 0 & (u_2)_j & (h_2)_j \\ rg & 0 & g & (u_2)_j \end{pmatrix},$$

where $(u_1)_j = (q_1)_j/(h_1)_j$ and $(u_2)_j = (q_2)_j/(h_2)_j$. We then compute the matrices Q_j and Q_j^{-1} numerically and implement the LCD of the equilibrium variables followed by the fifth-order Ai-WENO-Z interpolation giving $\mathbf{\Gamma}_{j \mp \frac{1}{2}}^\pm$ and then $\mathbf{E}_{j \mp \frac{1}{2}}^\pm = ((q_1)_{j \mp \frac{1}{2}}^\pm, (E_1)_{j \mp \frac{1}{2}}^\pm, (q_2)_{j \mp \frac{1}{2}}^\pm, (E_2)_{j \mp \frac{1}{2}}^\pm)^\top$. After that, we apply the same fifth-order Ai-WENO-Z interpolation to obtain the one-sided values of the bottom topography $Z_{j \mp \frac{1}{2}}^\pm$, and then solve the nonlinear equations as described in [5, Equations (3.11)–(3.14)] to obtain $(h_i)_{j+\frac{1}{2}}^\pm$ and $(\hat{h}_i)_{j+\frac{1}{2}}^\pm$, $i = 1, 2$.

4 Numerical Examples

In this section, we test the proposed fifth-order WB A-WENO scheme based on the LCD of equilibrium variables on several numerical examples for the nozzle flow system and one- and two-layer shallow water equations. For the sake of brevity, this scheme will be referred to as Scheme 1 and its performance will be compared with the following two schemes:

- Scheme 2: The WB A-WENO scheme from [5], in which the Ai-WENO-Z interpolation is applied to the equilibrium variables \mathbf{E} without any LCD;
- Scheme 3: The A-WENO scheme from [3], which can only preserve the simplest “lake-at-rest” steady states, but use the LCD applied to the conservative variables \mathbf{U} to reduce the spurious oscillations.

In all of the examples, we have solved the ODE system (2.1) using the three-stage third-order strong stability preserving (SSP) Runge-Kutta solver (see, e.g., [8,9]) with the time-step restricted by the CFL number 0.5.

4.1 Nozzle Flow System

Example 1—Flow in Continuous Divergent Nozzle

In the first example taken from [5,12], we consider the divergent nozzle described using the smooth cross-section

$$\sigma(x) = 0.976 + 0.748 \tanh(0.8x - 4).$$

We first take the steady states with $q_{\text{eq}}(x) \equiv 8$, $E_{\text{eq}}(x) \equiv 21.9230562619897$ and compute the discrete values of $\rho_{\text{eq}}(x)$ by solving the corresponding nonlinear equations; see [5,12]. We then obtain $u_{\text{eq}}(x) = q_{\text{eq}}(x)/(\sigma(x)\rho_{\text{eq}}(x))$.

Equipped with these steady states, we add a small perturbation to the density field and consider the initial data

$$\rho(x, 0) = \rho_{\text{eq}}(x) + \begin{cases} 10^{-2}, & x \in [0.5, 1.5], \\ 0, & \text{otherwise,} \end{cases} \quad q(x, 0) = \sigma(x)\rho(x, 0)u_{\text{eq}}(x),$$

which are prescribed in the computational domain $[0, 10]$ subject to the free boundary conditions.

We compute the numerical solutions until the final time $t = 0.8$ by Schemes 1–3 on a uniform mesh with $\Delta x = 1/20$ and plot the differences $\rho(x, 0.8) - \rho_{\text{eq}}(x)$ and $q(x, 0.8) - q_{\text{eq}}(x)$ in Figure 4.1. As one can see, Scheme 1 clearly outperforms Schemes 2 and 3 as there are no oscillations in the results computed by Scheme 1. We also stress that in this example, Scheme 3, which is not WB, produces the largest oscillations as we capture small perturbations of the steady state.

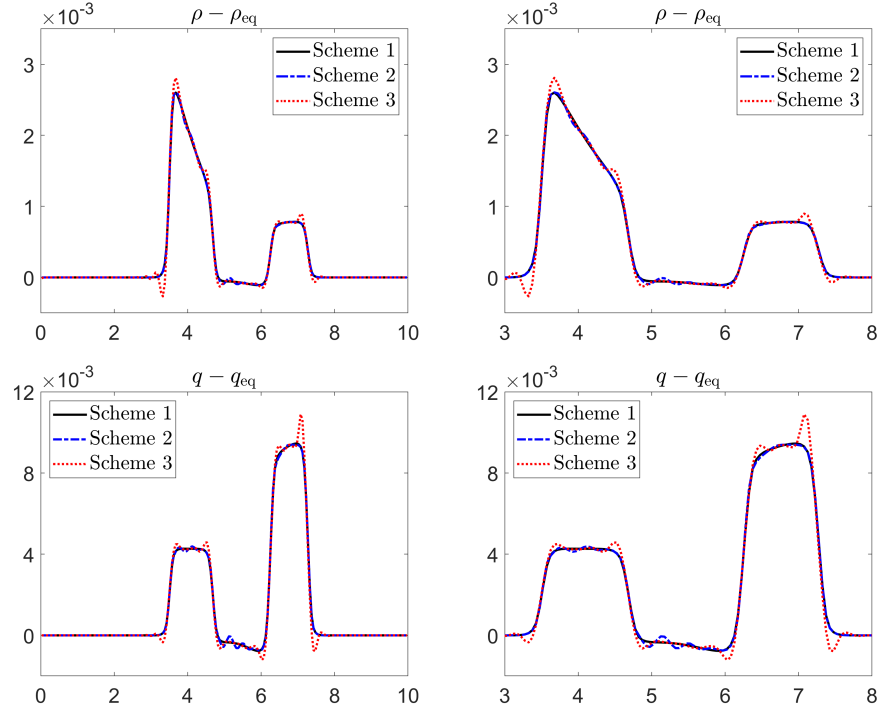


Figure 4.1: Example 1: The differences $\rho(x, 0.8) - \rho_{\text{eq}}(x)$ (top row) and $q(x, 0.8) - q_{\text{eq}}(x)$ (bottom row) computed by Schemes 1–3, and zoom at $x \in [3, 8]$ (right column).

Example 2—Flow in Continuous Convergent Nozzle

In the second example also taken from [5, 12], we consider the convergent nozzle described using the smooth cross-sections

$$\sigma(x) = 0.976 - 0.748 \tanh(0.8x - 4).$$

We first take the steady states with $q_{\text{eq}}(x) \equiv 8$, $E_{\text{eq}}(x) \equiv 58.3367745090349$, compute the discrete values of $\rho_{\text{eq}}(x)$ by solving the corresponding nonlinear equations, and then obtain $u_{\text{eq}}(x) = q_{\text{eq}}(x)/(\sigma(x)\rho_{\text{eq}}(x))$; see [5, 12]. We then consider the initial data containing a substantially larger perturbation than the one studied in Example 1:

$$\rho(x, 0) = \rho_{\text{eq}}(x) + \begin{cases} 0.3, & x \in [0.5, 1.5], \\ 0, & \text{otherwise,} \end{cases} \quad q(x, 0) = \sigma(x)\rho(x, 0)u_{\text{eq}}(x).$$

As in Example 1, the computational domain is $[0, 10]$ and the free boundary conditions are imposed.

We compute the numerical solutions until the final time $t = 0.5$ by Schemes 1–3 on a uniform mesh with $\Delta x = 1/20$ and plot the differences $\rho(x, 0.5) - \rho_{\text{eq}}(x)$ and $q(x, 0.5) - q_{\text{eq}}(x)$ in Figure

4.2. As one can see, Scheme 3 does not produce visible oscillations as the magnitude of the perturbation is apparently larger than the size of the truncation errors. On the contrary, Scheme 2, which does not use any LCD, now produces larger oscillations than in Example 1, where the size of perturbation was much smaller.

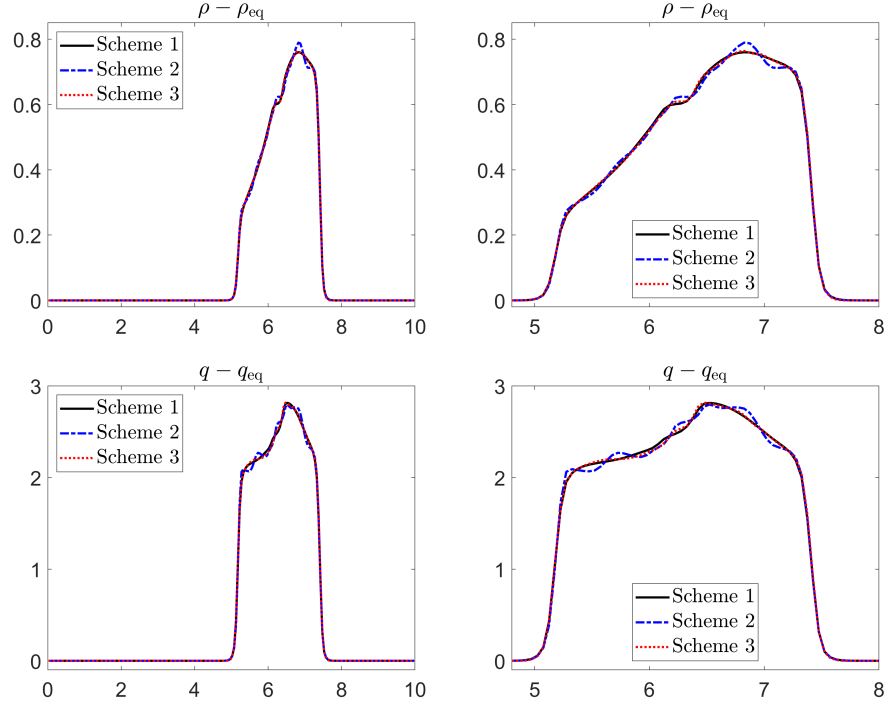


Figure 4.2: Example 2: The differences $\rho(x, 0.5) - \rho_{eq}(x)$ (top row) and $q(x, 0.5) - q_{eq}(x)$ (bottom row) computed by Schemes 1–3, and zoom at $x \in [4.8, 8]$ (right column).

4.2 Saint-Venant System with Manning Friction

Example 3—Riemann Problem (n=0.4)

In this example, we test the performance of Schemes 1–3 on a Riemann problem with the following initial data (prescribed in the computational domain $[-0.1, 0.3]$ subject to the free boundary conditions):

$$h(x, 0) = \begin{cases} 1, & x < 0, \\ 0.8, & x > 0, \end{cases} \quad u(x, 0) = \begin{cases} 2, & x < 0, \\ 4 & x > 0, \end{cases}$$

and the bottom topography also containing a jump at $x = 0$:

$$Z(x) = \begin{cases} 1, & x < 0, \\ 1.9 & x > 0. \end{cases}$$

We compute the numerical solutions by the three studied schemes until the final time $t = 0.03$ on a uniform mesh with $\Delta x = 1/250$. The obtained results (h , q , and E) are shown in Figure 4.3, where one can observe that the solutions computed by both Schemes 2 and 3 are oscillatory, whereas Scheme 1 solution is oscillation-free. In order to further study performance of Schemes

1–3, we refine the mesh to $\Delta x = 1/2500$ and compare the high-resolution solutions of the three studied schemes; see Figure 4.4. One can observe that the high-frequency oscillations produced by Scheme 3 on a coarse mesh, were almost suppressed when the mesh was refined, whereas Scheme 2, which does not employ any LCD, still produces oscillations, which can be clearly seen in the zoom views shown in the right column.

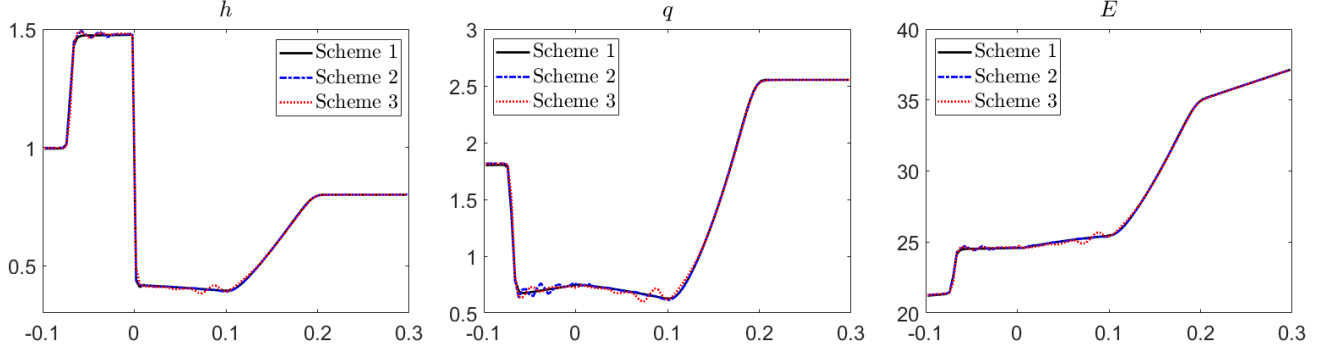


Figure 4.3: Example 3: Water depth h , discharge q , and energy E computed by Schemes 1–3 using $\Delta x = 1/250$.

Example 4—Convergence to a Steady State (n=0.15)

In this example, we study the convergence of the solutions computed by Schemes 1–3 towards the steady flow over a hump. We consider the continuous bottom topography given by

$$Z(x) = \begin{cases} 0.2 & \text{if } 8 \leq x \leq 12, \\ 0 & \text{otherwise,} \end{cases}$$

and the initial and boundary data that correspond to a subcritical flow:

$$h(x, 0) \equiv 2 - Z(x), \quad q(x, 0) \equiv 0, \quad q(0, t) = 4.42, \quad h(25, t) = 2,$$

with the boundary conditions for h at $x = 0$ and q at $x = 25$ set to be free.

We compute the numerical solutions until the final time $t = 500$ on the computational domain $[0, 25]$ covered by a uniform mesh with $\Delta x = 1/4$. The obtained numerical solutions ($h + Z$, q , and E) are plotted in Figure 4.5. One can clearly see that the WB Schemes 1 and 2 converge to the constant q and E , whereas the non-WB Scheme 3 generates oscillations, whose size is proportional to the size of the local truncation error.

We then test the ability of the studied schemes to capture the propagation of a small perturbation of the obtained moving-water equilibria. To this end, we denote the obtained steady states by $h_{\text{eq}}(x)$ and $q_{\text{eq}}(x)$ (notice that each scheme has its own discrete equilibrium), and then consider the following initial data:

$$h(x, 0) = h_{\text{eq}}(x) + \begin{cases} 10^{-4}, & 9.5 \leq x \leq 10.5, \\ 0, & \text{otherwise,} \end{cases} \quad q(x, 0) = q_{\text{eq}}(x).$$

We compute the solutions by the three studied schemes until the final time $t = 1.5$ on the same uniform mesh with $\Delta x = 1/4$. The obtained differences $h(x, 1.5) - h_{\text{eq}}(x)$ are plotted in Figure

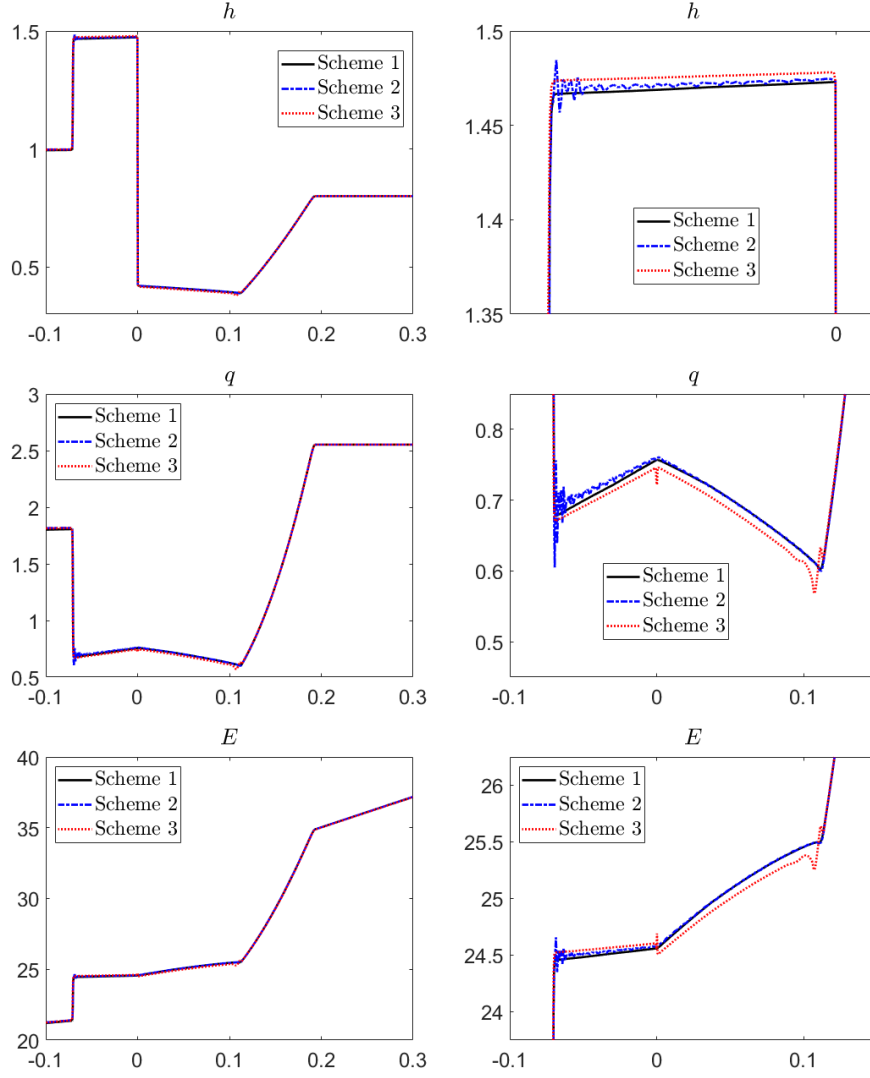


Figure 4.4: Example 3: Water depth h , discharge q , and energy E computed by Schemes 1–3 using $\Delta x = 1/2500$ (left column), and zoom at the areas containing oscillations in Scheme 2 solution (right column).

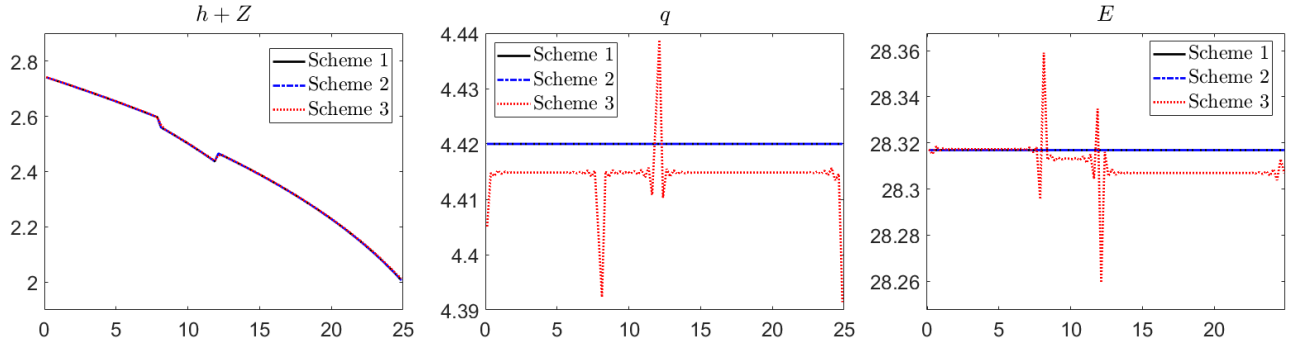


Figure 4.5: Example 4 (moving water steady state): $h + Z$, q , and E computed by Schemes 1–3.

4.6. One can clearly see that both the WB Schemes 1 and 2 can capture the time evolution of the perturbation quite accurately, whereas the non-WB Scheme 3 generates spurious oscillations as it can preserve still-water equilibria only. Even though Scheme 2 is WB, it still generates some oscillations, and thus Scheme 1 clearly outperforms both of its counterparts in this example.

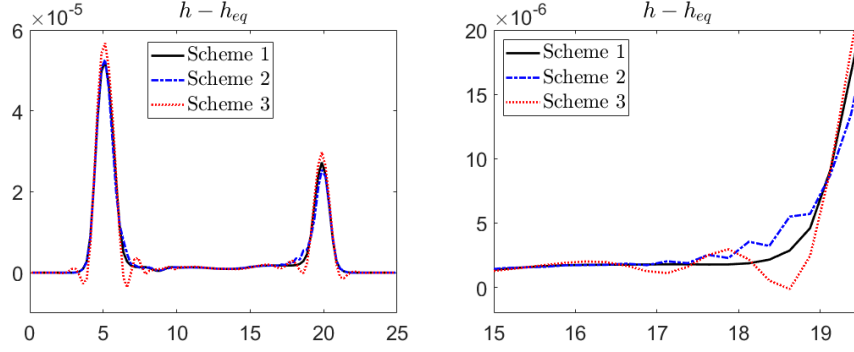


Figure 4.6: Example 4: The differences $h(x, 1.5) - h_{\text{eq}}(x)$ computed by Schemes 1–3 (left) and zoom at $x \in [15, 19.5]$ (right).

4.3 Two-Layer Shallow Water System

Example 5—Small Perturbation of Discontinuous Steady State

In the fifth example taken from [5, 12], we consider a discontinuous steady state given by

$$\begin{aligned} (h_1)_{\text{eq}}(x) &:= \begin{cases} 1.22373355048230, & x < 0, \\ 1.44970064153589, & x > 0, \end{cases} & (q_1)_{\text{eq}}(x) &\equiv 12, \\ (h_2)_{\text{eq}}(x) &:= \begin{cases} 0.968329515483846, & x < 0, \\ 1.12439026921484, & x > 0, \end{cases} & (q_2)_{\text{eq}}(x) &\equiv 10, \end{aligned}$$

and a discontinuous bottom topography

$$Z(x) = \begin{cases} -2, & x < 0, \\ -1, & x > 0. \end{cases}$$

In order to test the ability of the studied schemes to capture quasi-steady solutions, we add a small perturbation to the upper layer depth and take the following initial data:

$$\begin{aligned} h_1(x, 0) &= (h_1)_{\text{eq}}(x) + \begin{cases} 0.12, & x \in [-0.9, -0.8], \\ 0, & \text{otherwise,} \end{cases} \\ h_2(x, 0) &= (h_2)_{\text{eq}}(x), \quad q_1(x, 0) = (q_1)_{\text{eq}}(x), \quad q_2(x, 0) = (q_2)_{\text{eq}}(x), \end{aligned}$$

prescribed in the computational domain $[-1, 1]$ subject to the free boundary conditions.

We compute the numerical solutions until the final time $t = 0.08$ by Schemes 1–3 on a uniform mesh with $\Delta x = 1/100$. The differences $h_1(x, 0.08) - (h_1)_{\text{eq}}(x)$ and $h_2(x, 0.08) - (h_2)_{\text{eq}}(x)$ are plotted in Figure 4.7, where one can clearly see that, unlike the proposed Scheme 1, Schemes 2 and 3 produce oscillatory numerical results.

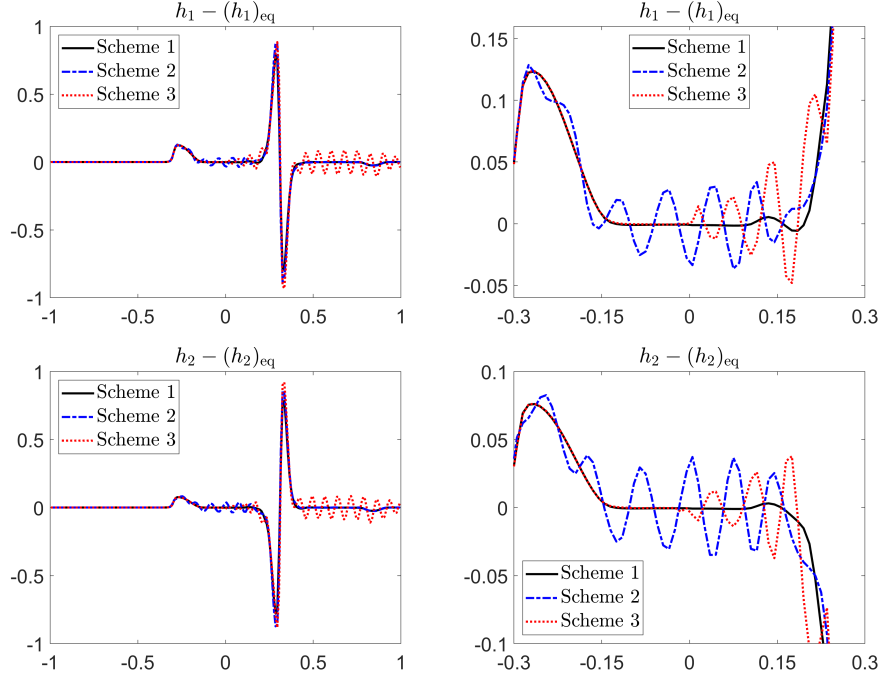


Figure 4.7: Example 5: The differences $h_1(x, 0.08) - (h_1)_{\text{eq}}(x)$ (top row) and $h_2(x, 0.08) - (h_2)_{\text{eq}}(x)$ (bottom row), and zoom at $x \in [-0.3, 0.3]$ (right column).

Example 6—Riemann Problem

In the last example taken from [5, 12], we numerically solve a Riemann problem with the following initial data:

$$(h_1, q_1, h_2, q_2)(x, 0) = \begin{cases} (1, 1.5, 1, 1), & x < 0, \\ (0.8, 1.2, 1.2, 1.8), & \text{otherwise,} \end{cases}$$

and discontinuous bottom topography:

$$Z(x) = \begin{cases} -2, & x < 0, \\ -1.5, & \text{otherwise,} \end{cases}$$

prescribed in the computational domain $[-1, 1]$ subject to free boundary conditions.

We compute the numerical solutions until the final time $t = 0.1$ by Schemes 1–3 on a uniform mesh with $\Delta x = 1/50$. The obtained upper layer depth h_1 and lower layer depth h_2 are plotted in Figure 4.8, where one can see that Scheme 1 clearly outperforms Schemes 2 and 3 as there are no oscillations in the results computed by Scheme 1.

Remark 4.1 *In the above examples, we have shown that reconstructing equilibrium variables through the LCD is advantageous as it helps to remove WENO-type oscillations while keeping the scheme WB. The proposed LCD of the equilibrium variables is based on the projections onto the eigenvectors of the matrices $C_j = C(\mathbf{U}_j)$ as explained in §3. Instead, one may try to base the LCD of equilibrium variables on the eigenvectors of the matrices $\mathbf{A}_j = \mathbf{A}(\mathbf{U}_j) := \partial \mathbf{F} / \partial \mathbf{U}(\mathbf{U}_j) - B(\mathbf{U}_j)$. To this end, one needs to compute the matrices \hat{Q}_j and \hat{Q}_j^{-1} such that $\hat{Q}_j^{-1} \mathbf{A}_j \hat{Q}_j$ is a diagonal matrix, and then to apply the Ai-WENO-Z interpolation to a different set of the local characteristic*

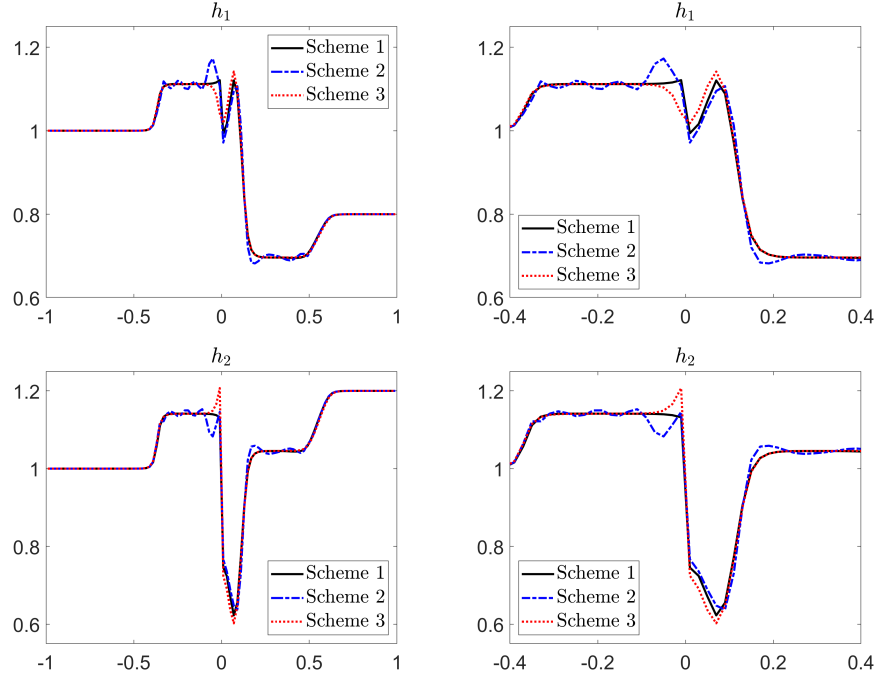


Figure 4.8: Example 6: Upper layer depth h_1 (top row) and lower layer depth h_2 (bottom row), and zoom at $x \in [-0.4, 0.4]$ (right column).

variables $\hat{\Gamma}_k$, which are defined by

$$\hat{\Gamma}_k = \hat{Q}_j^{-1} \mathbf{E}_k, \quad k = j \pm 2, j \pm 1, j.$$

The Ai-WENO-Z reconstruction then gives $\hat{\Gamma}_{j \pm \frac{1}{2}}^\pm$ and hence $\mathbf{E}_{j \pm \frac{1}{2}}^\pm = \hat{Q}_j \hat{\Gamma}_{j \pm \frac{1}{2}}^\pm$, which are different from the values $\mathbf{E}_{j \pm \frac{1}{2}}^\pm$ obtained in (3.1)–(3.2).

However, this kind of LCD does not lead to very good results. To demonstrate this, we recompute the numerical solutions in Examples 2, 4, and 5 using Scheme 1, but with an aforementioned alternative LCD based on $\mathcal{A}(\mathbf{U})$ rather than $C(\mathbf{U})$. The obtained results shown in Figures 4.9–4.12 confirm the advantages of the LCD based on $C(\mathbf{U})$.

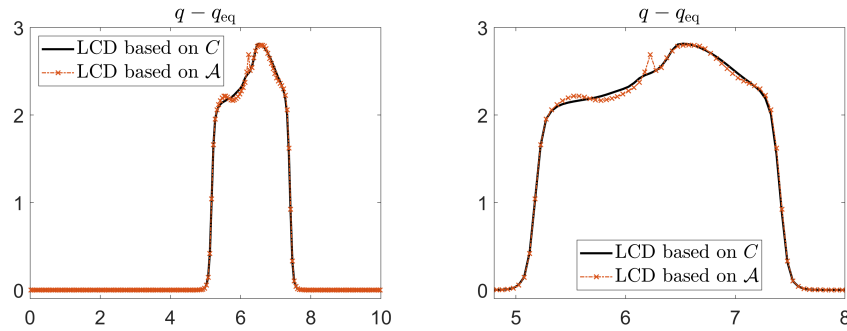


Figure 4.9: Example 2: The differences $q(x, 0.5) - q_{\text{eq}}(x)$ computed by Scheme 1 with two different LCD of the equilibrium variables (left) and zoom at $x \in [4.8, 8]$ (right).

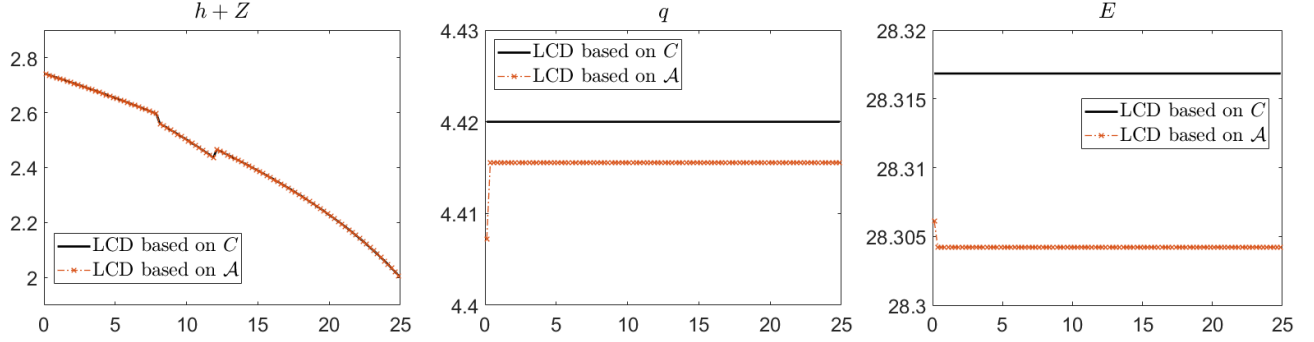


Figure 4.10: Example 4 (moving water steady state): $h + Z$, q , and E computed by Scheme 1 with two different LCD of the equilibrium variables.

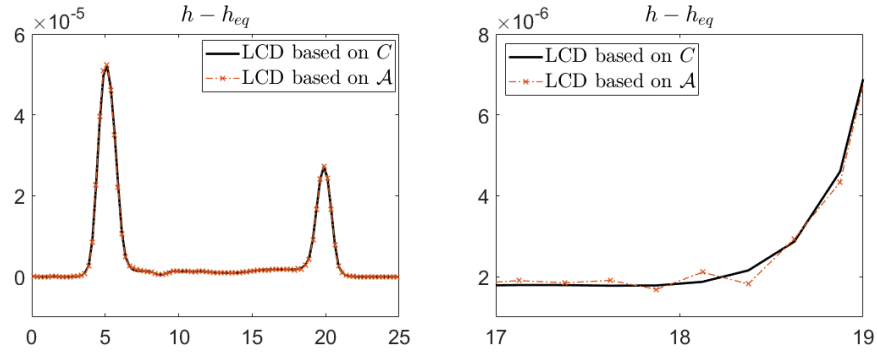


Figure 4.11: Example 4: The differences $h(x, 1.5) - h_{\text{eq}}(x)$ computed by Scheme 1 with two different LCD of the equilibrium variables (left) and zoom at $x \in [17, 19]$ (right).

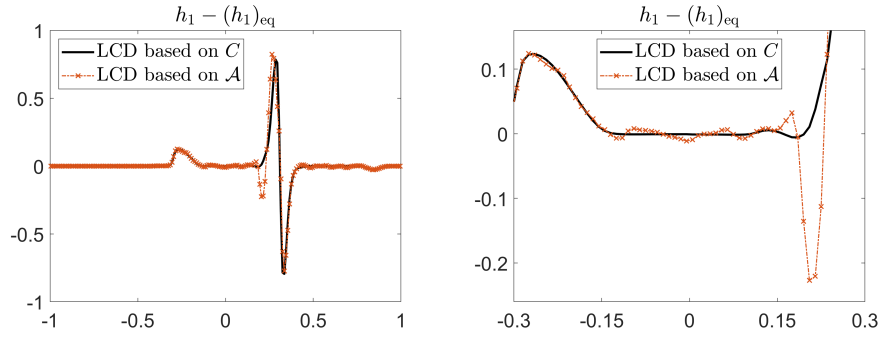


Figure 4.12: Example 5: The differences $h_1(x, 0.12) - (h_1)_{\text{eq}}$ computed by Scheme 1 with two different LCD of the equilibrium variables (left) and zoom at $x \in [-0.3, 0.3]$ (right).

Acknowledgment

The work of S. Chu was supported in part by the DFG (German Research Foundation) through HE5386/19-3, 27-1. The work of A. Kurganov was supported in part by NSFC grant 12171226 and by the fund of the Guangdong Provincial Key Laboratory of Computational Science and Material Design (No. 2019B030301001).

References

- [1] Y. CAO, A. KURGANOV, Y. LIU, AND R. XIN, Flux globalization based well-balanced path-conservative central-upwind schemes for shallow water models, *J. Sci. Comput.*, 92 (2022). Paper No. 69.
- [2] A. CHERTOCK, S. CHU, AND A. KURGANOV, Adaptive high-order A-WENO schemes based on a new local smoothness indicator, *E. Asian. J. Appl. Math.*, 13 (2023), pp. 576–609.
- [3] S. CHU, A. KURGANOV, AND M. NA, Fifth-order A-WENO schemes based on the path-conservative central-upwind method, *J. Comput. Phys.*, 469 (2022). Paper No. 111508.
- [4] S. CHU, A. KURGANOV, AND R. XIN, New more efficient A-WENO scheme. Preprint available at <https://sites.google.com/view/alexander-kurganov/publications>.
- [5] S. CHU, A. KURGANOV, AND R. XIN, A well-balanced fifth-order A-WENO scheme based on flux globalization, *Beijing J. Pure Appl. Math.* To appear.
- [6] W. S. DON, D.-M. LI, Z. GAO, AND B.-S. WANG, A characteristic-wise alternative WENO-Z finite difference scheme for solving the compressible multicomponent non-reactive flows in the overestimated quasi-conservative form, *J. Sci. Comput.*, 82 (2020). Paper No. 27.
- [7] W. S. DON, R. LI, B.-S. WANG, AND Y. H. WANG, A novel and robust scale-invariant WENO scheme for hyperbolic conservation laws, *J. Comput. Phys.*, 448 (2022). Paper No. 110724.
- [8] S. GOTTLIEB, D. KETCHESON, AND C.-W. SHU, Strong stability preserving Runge-Kutta and multistep time discretizations, World Scientific Publishing Co. Pte. Ltd., Hackensack, NJ, 2011.
- [9] S. GOTTLIEB, C.-W. SHU, AND E. TADMOR, Strong stability-preserving high-order time discretization methods, *SIAM Rev.*, 43 (2001), pp. 89–112.
- [10] Y. JIANG, C.-W. SHU, AND M. ZHANG, An alternative formulation of finite difference weighted ENO schemes with Lax-Wendroff time discretization for conservation laws, *SIAM J. Sci. Comput.*, 35 (2013), pp. A1137–A1160.
- [11] E. JOHNSON, On the treatment of contact discontinuities using WENO schemes, *J. Comput. Phys.*, 230 (2011), pp. 8665–8668.
- [12] A. KURGANOV, Y. LIU, AND R. XIN, Well-balanced path-conservative central-upwind schemes based on flux globalization, *J. Comput. Phys.*, 474 (2023). Paper No. 111773.
- [13] P. LI, T. T. LI, W. S. DON, AND B.-S. WANG, Scale-invariant multi-resolution alternative WENO scheme for the Euler equations, *J. Sci. Comput.*, 94 (2023). Paper No. 15.
- [14] H. LIU, A numerical study of the performance of alternative weighted ENO methods based on various numerical fluxes for conservation law, *Appl. Math. Comput.*, 296 (2017), pp. 182–197.
- [15] R. MANNING, On the flow of water in open channel and pipes, *Transactions of the Institution of Civil Engineers of Ireland*, 20 (1891), pp. 161–207.

- [16] T. NONOMURA AND K. FUJII, Characteristic finite-difference WENO scheme for multicomponent compressible fluid analysis: overestimated quasi-conservative formulation maintaining equilibriums of velocity, pressure, and temperature, *J. Comput. Phys.*, 340 (2017), pp. 358–388.
- [17] J. QIU AND C.-W. SHU, On the construction, comparison, and local characteristic decomposition for high-order central WENO schemes, *J. Comput. Phys.*, 183 (2002), pp. 187–209.
- [18] C.-W. SHU, Essentially non-oscillatory and weighted essentially non-oscillatory schemes, *Acta Numer.*, 5 (2020), pp. 701–762.
- [19] B.-S. WANG AND W. S. DON, Affine-invariant WENO weights and operator, *Appl. Numer. Math.*, 181 (2022), pp. 630–646.
- [20] B.-S. WANG, W. S. DON, N. K. GARG, AND A. KURGANOV, Fifth-order A-WENO finite-difference schemes based on a new adaptive diffusion central numerical flux, *SIAM J. Sci. Comput.*, 42 (2020), pp. A3932–A3956.
- [21] B.-S. WANG, W. S. DON, A. KURGANOV, AND Y. LIU, Fifth-order A-WENO schemes based on the adaptive diffusion central-upwind Rankine-Hugoniot fluxes, *Commun. Appl. Math. Comput.*, 5 (2023), pp. 295–314.
- [22] B.-S. WANG, P. LI, Z. GAO, AND W. S. DON, An improved fifth order alternative WENO-Z finite difference scheme for hyperbolic conservation laws, *J. Comput. Phys.*, 374 (2018), pp. 469–477.